Journal of Materials Chemistry C

ROYAL SOCIETY OF CHEMISTRY

REVIEW

View Article Online
View Journal | View Issue

Cite this: J. Mater. Chem. C, 2022, 10, 2349

Flexible transparent electrodes based on metallic micro–nano architectures for perovskite solar cells

Yongrui Yang, [ab] Yang Wang, [ab] Yali Qiao *[ab] and Yanlin Song *[ab]

Received 31st August 2021,
Accepted 12th October 2021

DOI: 10.1039/d1tc04101k

rsc.li/materials-c

With the development of lightweight and flexible electronics, flexible transparent electrodes (TEs) have attracted huge attention in both academia and industry, and play a central role in high-performance flexible electronics. As a kind of emerging conducting material for TEs, metallic micro–nano architectures (MMNAs) possess both low sheet resistance and high optical transmittance. In addition, the high flexibility and low-cost solution processing make MMNAs promising candidates to replace the traditional conductive metal oxides, which suffer from the high-cost fabrication process and low conductivity on flexible substrates. In this review, we summarize the recent progress in flexible TEs based on MMNAs, as well as the comparison to other conducting materials, such as conducting polymers, graphene, carbon nanotubes, *etc.* Specially, we highlight the applications of flexible TEs based on MMNAs in perovskite solar cells (PSCs), including inverted PSCs, conventional PSCs, and semi-transparent PSCs. Finally, the challenges and prospects in this field are proposed.

1. Introduction

Hybrid metal halide perovskite materials have been one of the most promising candidates as light-active layers in thin-film photovoltaics since the first use of perovskite in dye-sensitized solar cells in 2009.[1–7] To accomplish light-weight wearable electronics, the rapid emergence of flexible thin-film perovskite photovoltaics, such as perovskite solar cells (PSCs),[8–12] photodetectors (PDs),[13–16] and perovskite light-emitting diodes (PLEDs),[17–20] has increased a tremendous demand for developing flexible transparent electrodes (TEs) with low sheet resistance, high optical transmittance, and robust flexibility. Currently, the most widely used TEs in high-performance perovskite photovoltaics are transparent conducting oxides (TCOs) fabricated by vacuum deposition, such as indium tin oxide (ITO)[4,21,22] and fluorine-doped tin oxide (FTO).[23,24] Unfortunately, the large modulus and small Poisson ratio of TCOs lead to the easy occurrence of cracks when TCOs are coated on flexible substrates,[25] such as polyethylene terephthalate (PET)

[a] Key Laboratory of Green Printing, CAS Research/Education Center for Excellence in Molecular Sciences, Institute of Chemistry, Chinese Academy of Sciences, Zhongguancun North First Street 2, 100190 Beijing, P. R. China. E-mail: qiaoyl@iccas.ac.cn, ylsong@iccas.ac.cn
[b] University of Chinese Academy of Sciences, 100049 Beijing, P. R. China

Yongrui Yang

Yongrui Yang received his Master degree from the School of Polymer Science and Polymer Engineering, University of Akron (USA), in 2020. Now he is a PhD candidate in the Institute of Chemistry, Chinese Academy of Sciences (ICCAS), under the supervision of Prof. Yanlin Song and Prof. Yali Qiao. His research interest includes perovskite photovoltaics and transparent electrodes.

Yang Wang

Yang Wang received his PhD degree in materials physics and chemistry from Beihang University in 2016. Now he is an associate professor at the Key Laboratory of Green Printing, ICCAS. His research interests include organic–inorganic hybrid optoelectronics such as solar cells, printing photoelectric devices and photo detectors.

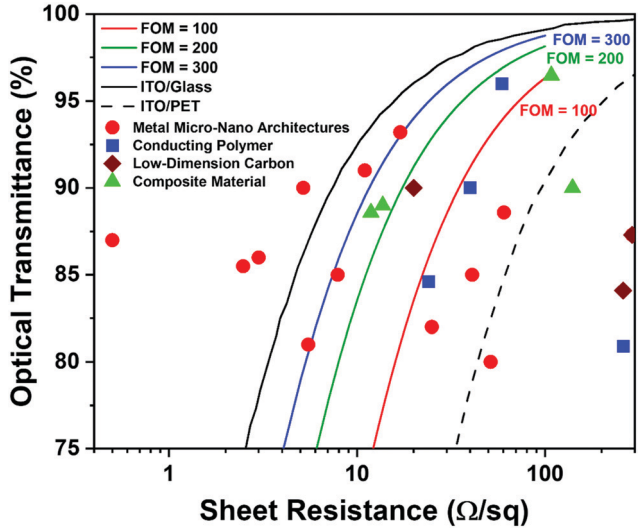

Fig. 1 Sheet resistance and optical transmittance of different conductive materials.

and polyethylene naphthalate (PEN).[11,26,27] These degradations from TEs make the performance of flexible perovskite photovoltaics still lag compared to the ones fabricated on rigid substrates.[9,28–32] What's more, the vacuum deposition processing of TCOs also suffers from the high processing temperature (usually over 200 °C), low throughput and scarcity of indium, which is incompatible with the high throughput solution-processing and printing technologies.[25,33–36]

To address the abovementioned drawbacks, a variety of novel materials, such as metallic micro–nano architectures (MMNAs),[37–47] conducting polymers,[48–53] low-dimensional carbons,[54–58] and the composites formed by these materials,[49,59–64] have been developed as promising candidates for flexible TEs. Fig. 1 shows the sheet resistance and optical transmittance of different conductive materials recently reported.[10,40,41,52,56,61,65–82] The FoM value is the factor to evaluate the performance of TEs, which can be calculated using eqn (1):[44,52]

$$\mathrm{FoM} = \frac{188.5\Omega}{R_s \times (T(\lambda)^{-0.5} - 1)} \quad (1)$$

where R_s is the sheet resistance and $T(\lambda)$ is the optical transparency at a specified wavelength. A higher FoM value suggests that the TEs possess lower sheet resistance and higher transmittance. Four key factors should be possessed by the flexible TEs for the perovskite photovoltaics: (1) low sheet resistance to decrease the total series resistance of the photovoltaic devices; (2) high optical transmittance to guarantee the incident photons absorbed by a photo-active layer as much as possible; (3) low surface roughness to prevent the current shortage and leakage; and (4) robust mechanical flexibility on the flexible substrate. Besides these four key factors, appropriate work function, cost-effective material, high-throughput fabrication processing, and chemical stability should also be considered for developing high-performance flexible TEs. Among the abovementioned novel conductive materials, MMNAs have been widely equipped in silicon solar cells,[83,84] III–V photovoltaics,[85,86] Cu(In,Ga)(Se,S)$_2$ cells,[87–89] and organic solar cells,[44,90–92] due to the high conductivity and tunable optical transmittance of MMNAs. However, drawbacks including high roughness, immigration of metallic ions, and degradation at the interface are faced when flexible TEs based on MMNAs are integrated with PSCs.

In this review, we focus on the role played by MMNA TEs in flexible PSCs, particularly in critical issues in different PSC device configurations. A brief introduction related to different novel conductive materials including MMNAs, conducting polymers, and low-dimensional carbons are given in Section 2.1. The MMNA TEs are discussed in Section 2.2 including chemical components, physical morphology, and fabrication methods. In Section 3, the MMNA TEs in different PSC device configurations involving inverted, conventional, and semitransparent structures are reviewed, especially in the metal ion immigration and interface charge transportation. Finally, we give our discussion and outlook about this area in Section 4.

Yali Qiao

Yali Qiao received her PhD degree at ICCAS in 2011. Later, she conducted postdoctoral research at the University of South Carolina and Columbia University. She joined the Key Laboratory of Green Printing at ICCAS as a professor in 2018. Her research interests include the development of high-resolution patterning technology, the patterning of organic and composite functional materials and their applications in electronic/optoelectronic devices.

Yanlin Song

Yanlin Song received his PhD degree from the Department of Chemistry at Peking University in 1996. Then he conducted research as a postdoctoral follow at Tsinghua University from 1996 to 1998. He has been working at ICCAS since 1998. His research interests include nano-materials and green-printing technology, printed electronics and photonics, fabrication and applications of photonic crystals. He has published more than 400 papers, 14 books and chapters, and has been granted more than 130 patents from China, USA, European Union, Japan, Korea, etc.

2. Comparison between MMNAs and other conductive materials

2.1. TCOs, conducting polymers, and low-dimensional carbons

2.1.1. TCOs. As mentioned before, rigid PSCs based on TCO electrodes have already achieved high PCE which is almost comparable to the value in single-crystal silicon-based solar cells. The most widely used indium tin oxide (ITO) and fluorine-doped tin oxide (FTO) present an excellent conductivity of around 10^4–10^5 S cm^{-1}. The electrodes based on ITO or FTO show a low sheet resistance less than 20 Ω sq^{-1} at more than 85% average optical transmittance from 375 to 1000 nm. These TCO materials are usually fabricated by magnetron sputtering and vacuum deposition.[93,94] The scarcity of indium, low material utilization, and high vacuum during the sputtering process make ITO electrodes take a considerable part of the cost in some thin-film photovoltaics.[95,96] To overcome the high-cost fabrication process, solution-processed TCO thin films were developed by using the sol–gel method or directly depositing TCO nanoparticles.[97–99] However, after being deposited by solution-processing, the films still need to be thermally annealed at high temperatures (300–500 °C) to remove organic protective agents and enhance the crystallinity of TCOs. For example, Romanyuk *et al.* developed a solution-processed ITO thin film by spin-coating ethanolamine-modified ITO nanoparticles on the substrates.[99] The ITO films achieved a conductivity of 43 S cm^{-1} and more than 90% optical transmittance in the wavelength range from 380 nm to 1100 nm. Nevertheless, the films still need to be annealed at 300 °C, which is inadaptable to the polymer-based flexible substrates. Besides the high-temperature fabrication processing, the fragile nature also makes TCOs doomed to be incompatible with flexible substrates.

2.1.2. Conducting polymers. For the conducting polymers for transparent electrodes, the most widely reported material is poly(3,4-ethylenedioxythiophene) polystyrene sulfonate (PEDOT:PSS). PEDOT as a kind of well-developed oxidized polythiophene presents a good conductivity of around 1–10^3 S cm^{-1} with promising optical transmittance.[100–102] After being coupled with PSS, the insoluble PEDOT can be dissolved in water at an appreciable solubility, which provides great potential in solution-processing and high-throughput roll-to-roll (R2R) printing. However, the parasitic absorption of PEDOT:PSS is an obstruction to photons in the absorption by active layers, which leads to decreased current in solar cells.[103–105] To address the influence from the parasitic absorption of PEDOT:PSS, a variety of methods such as decreasing the content of PEDOT:PSS in TEs[103,106] and chemical doping[104] have been developed. What's more, with the enhancement in solubility, the nonconducting PSS decreases the electrical conductivity of PEDOT:PSS composites compared to that in pure PEDOT.[107,108] To obtain higher electrical conductivity, plenty of efforts have been made. For example, Bao *et al.* investigated a series of ionic additives for PEDOT:PSS.[52] These ionic additives enable PEDOT:PSS to show a more regulated π–π stacking morphology and also served as chemical dopants to boost the conductivity of PEDOT:PSS. The corresponding PEDOT:PSS thin film achieved an electrical conductivity of 4100 S cm^{-1} and a fracture strain of 800%. Although there are a large number of reports related to electrical conductivity enhancement of conducting polymers, the conductivity of conducting polymers still lags compared to that in TCOs, which will increase the total series resistance of photovoltaic devices.[10,101,109]

2.1.3. Low-dimensional carbons. Low-dimensional carbons, such as carbon nanotubes (CNTs), graphene, and reduced graphene oxides (rGO), are another promising conductive material for flexible TEs, due to the huge abundance of carbon on the earth, high optical transmittance, and solution-processable potential. However, the further flourishing of low-dimensional carbons in transparent TEs suffers from the high sheet resistance (usually more than 100 Ω sq^{-1}) and a high-cost fabrication process. For carbon nanotubes, the growth, dissociation, and purification of metallic single-wall carbon nanotubes (SWCNTs) are the key to achieve high electrical conductivity.[110–112] For instance, Liu *et al.* reported a high concentration of metallic SWCNTs by using hydrogen as an etchant gas to remove the semiconducting SWCNTs.[112] The thin film fabricated by metallic SWCNTs showed a sheet resistance of 84 Ω sq^{-1} at a transmittance of 82%. Graphene presented an ultra-transparency, quite a low surface roughness, and worthy electrical conductivity.[113,114] The electrical conductivity of graphene can be enhanced by chemical doping.[81,115,116] Im *et al.* developed a flexible electrode based on bis(trifluoromethanesulfonyl)-amide doped graphene.[116] The electrodes showed a sheet resistance of around 108 Ω sq^{-1} with an optical transmittance of 96.48% at 550 nm. The flexible PSCs based on this electrode reached a PCE of 18.3%. Compared to chemical vapor deposition graphene, the rGO fabricated by exfoliating graphite is accessible in the solution process.[117,118] In a word, the CVD fabrication process and high sheet resistance are still the main obstacles between low-dimensional carbon materials and high-performance flexible TEs.

2.2. Metallic micro–nano architectures

MMNAs formed by silver (Ag),[39,119–123] copper (Cu),[124–126] gold (Au),[37,127,128] platinum (Pt),[129] nickel (Ni),[65,130] or zinc (Zn)[89] keep the high electrical conductivity from bulk metal and tunable optical transmittance in a wide range. In this way, varieties of MMNAs are regarded as the most potential conductive materials for flexible TEs.[35,36,131] The MMNAs can be divided into two main categories: random architectures and ordered architectures. TEs based on random MMNAs can be fabricated by a solution-process, which promises high-throughput production. However, when serving as TEs in thin-film photovoltaics, the inhomogeneous aggregation of MMNAs will cause current leakage and the degradation of device performance.[35,36,47] Compared to random MMNAs, ordered MMNAs with regular micro–nano primary cells and periods provide the homogeneous charge transport pathway in thin-film photovoltaics. The bottleneck for TEs based on ordered MMNAs is the high-resolution fabrication methods, such as self-assembling,[82] lithographic imprinting,[132,133] laser direct writing,[65,134] and electrochemical deposition,[135,136] which are incompatible with the high-throughput R2R process.

In this section, we will discuss the categories, fabrication methods, and electrical performance for both random and ordered MMNAs.

2.2.1. Random MMNAs. Random MMNAs usually include four different morphologies: nanoparticles (NPs),[137] nanowires (NWs),[126,127,138–141] nanorings (NRs),[142,143] and random grids[46] (as shown in Fig. 2). Different morphologies are caused by different growth behaviors of nanomaterials and the deposition process. Wiely *et al.* investigated the anisotropic growth mechanism of metal nanocrystals in solution by electrochemical measurements.[144] They found that the facet-selective anisotropic growth of metal nanostructures can be induced by the chloride ions. The reduction product of Cu^{2+} in the solution of hexadecylamine and ascorbic acid only presented a spherical particle morphology (Fig. 2a), when $Cu(NO_3)_2$ was used as the Cu source. After adding chloride ions, the hexadecylamine can selectively be adsorbed onto the (100) facets of Cu leading to an anisotropic growth of CuNWs along with (111) facets (Fig. 2b). Azani *et al.* developed a solvothermal method to synthesise silver nanorings.[142,143] When the pressure of the reactor increased to 150 kPa, 90% of the reduction product was silver nanorings as shown in Fig. 2c. The unbalanced pressure at the liquid–air interface assisted the AgNWs in keeping bent shapes. Random metal grids can be fabricated by the assembling or printing of metal NPs. For example, Kim *et al.* fabricated the random Ag grids by self-assembling AgNPs (Fig. 2d).[46] After self-assembling Ag grids on the substrate, the Ag grids were further embedded within PET substrates to form intaglio transparent electrodes. The corresponding electrode showed a sheet resistance of 3.95 Ω sq^{-1} and an average transmittance of 82.3%.

Among these random MMNAs, AgNWs are most widely reported as the transparent electrodes in thin-film photovoltaics. The solution-processed polyol synthesis established by Xia *et al.* anisotropic reduced Ag^+ along with (111) facets by ethylene glycol with the assistance of polyvinylpyrrolidone (PVP) (Fig. 3a).[145,146] This method can produce a significant amount of AgNWs at low cost. But to enhance the electrical conductivity to the same level as bulk metals, there still some modifications should be adopted. One of the minuses of electrical conductivity originates from the junction resistance shown in Fig. 3b.[38] Many efforts, such as thermal welding,[147–149] plasmonic welding,[150,151] and chemical welding,[44,152] have been used to weld AgNWs together. For example, Cho *et al.* used halide ions to weld the AgNWs.[38] As shown in Fig. 3b and c, in the halide ion solutions, the AgNWs can be slowly dissolved into Ag^+. The Ag^+ ions will redeposit near the junction where the electrostatic potential is higher than other regions. These Ag^+ ions can result in a strong fusion in the junction. After the wires were welded together, the sheet resistance sharply decreased from 24 to 9.8 Ω sq^{-1}. Junction welding efficiently decreases the sheet resistance of the AgNW electrodes. However, welding by heating and plasmonic welding usually cause high temperature (over 150 °C), which is not compatible with polymer-based substrates, and chemical welding always left the isolated chemical flux. In order to get AgNW electrodes with lower sheet resistance, synthesizing AgNWs with higher aspect ratios is another proved method.[153,154] The aspect ratio of AgNWs can be increased by the optimization of the polyol process.[154,155] For example, Hu *et al.* adopted a mixed PVP hydrogel as a capping ligand to suppress the formation of extra AgNPs.[155] The synthesized AgNWs present an average length of 78.5 μm, an average diameter of 63.8 nm, and an aspect ratio of 1200 (Fig. 3d and e). Besides the sheet resistance, transmittance is another key factor to evaluate the performance of TEs. For solution-processed AgNW electrodes, the optical transmittance can be easily tuned by the concentration of AgNW dispersion, in other words, the density of AgNWs. As shown in Fig. 3f and g, with the reduction of the AgNW density, the transmittance of the AgNW electrodes strikingly increased, meanwhile the sheet resistance also increased.[38] Thus, there is a trade-off between the sheet resistance and optical transmittance.

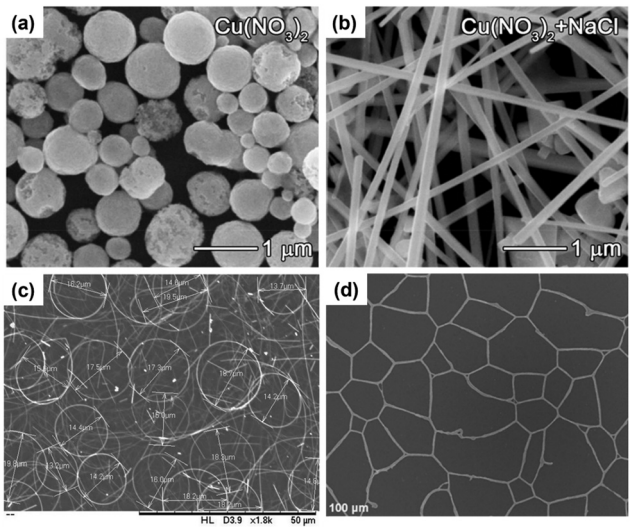

Fig. 2 Different morphologies of random MNMAs. (a) Nanoparticles. (b) Nanowires. Reproduced with permission from ref. 144. Copyright©2018, American Chemical Society. (c) Nanorings. Reproduced with permission from ref. 142. Copyright©2019, AIP Publishing LLC. (d) Random meshes. Reproduced with permission from ref. 46. Copyright©2016, Elsevier B.V.

2.2.2. Ordered MMNAs. Ordered MMNAs are a kind of metal mesh or grid with regular micro–nano primary cells and periods. The metal grids can be fabricated by ink-jet printing,[156–158] screen printing,[159] gravure printing,[43,160,161] self-assembling,[82] lithographic imprinting,[132,133] laser direct writing,[65,134] electrochemical deposition,[135,136] thermal evaporation,[162] or the combination process of these methods.[163,164] Among these methods, printing methods are widely used to fabricate flexible metal grids, due to the low processing temperature and large-scale accessibility.[68] Li *et al.* developed flexible Ag-mesh based on pre-etched PET substrates by lithographic imprinting as shown in Fig. 4a.[68,121] The line-width and period of the Ag mesh can be tuned by the pre-etched channels on the PET substrates. The intaglio transparent electrodes were further combined with highly conductive PEDOT:PSS to decrease the surface roughness. The PSCs based on Ag-mesh/PEDOT:PSS TEs (Fig. 4b) reached a champion PCE of 14% and 95.4% of the initial PCE after 5000 bending cycles.[68] The lithographic imprinting

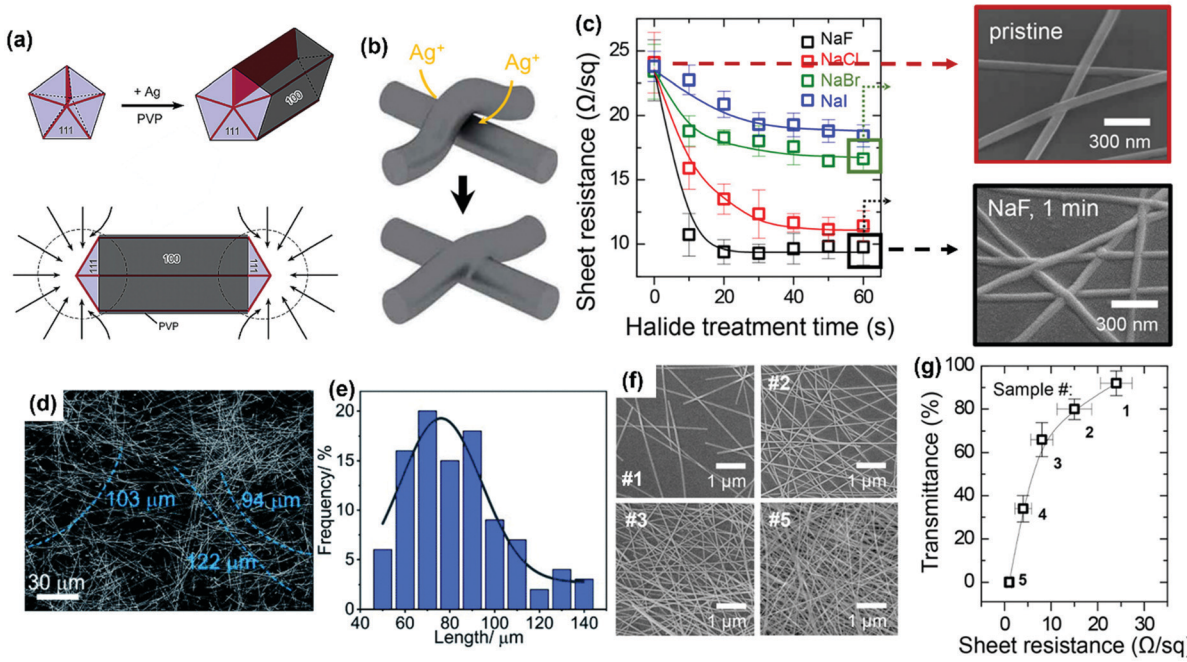

Fig. 3 (a) Schematic illustration of the growth of silver nanowires. Reproduced with permission from ref. 146. Copyright©2003, American Chemical Society. (b) Schematic diagram of the halide welding process. (c) Sheet resistance of the halide-welded AgNWs as a function of the treatment time. Reproduced with permission from ref. 38. Copyright©2017, American Chemical Society. (d) SEM image, (e) length distribution of AgNWs with a high aspect ratio. Reproduced with permission from ref. 155. Copyright©2020, Royal Society of Chemistry. (f) SEM images of AgNWs with different densities. (g) Sheet resistance and transmittance of AgNWs with different densities. Reproduced with permission from ref. 38. Copyright©2017, American Chemical Society.

fabrication process realized the large-scale flexible electrodes based on the Ag-mesh with a satisfactory surface roughness. However, during this method, 90% metallic ink were not filled into the pre-etched channels and washed out, which will increase the cost of electrodes. In addition, the up-bottom-filled AgNPs cannot compactly stack in the pre-etched channels. The vacancies among AgNPs enhance the sheet resistance of the electrodes and act as traps that harm the performance of photovoltaics. Self-assembling is a bottom-up method that can be used to fabricate compact Ag grids with almost 100% utilization of metallic inks. For example, Song *et al.* adopted confined bubbles as templates to self-assemble the flexible Ag grids.[82] As shown in Fig. 4c, the compact Ag grids can be assembled with a hexagonal primary cell. The flexible electrodes achieved a sheet resistance of 7.9 Ω sq^{-1} with 85% substrate-included optical transmittance. The self-assembled Ag-grid electrodes present outstanding sheet resistance and transmittance, but the massive production is still challenged, especially in the combination with roll-to-roll (R2R) processing. Besides Ag based metallic grids, Ni is another promising element for conducting a metallic network, due to the favorable electrical conductivity and large abundance in crust. Wang *et al.* investigated transparent electrodes based on embedded nickel meshes by electrochemical deposition.[65] Fig. 4d and e displays the Ni mesh and Ag mesh fabricated by electrochemical deposition and UV nanoimprinting lithography, respectively. The Ni mesh presented a significantly dense line compared to the Ag mesh, which leads to an ultra-low sheet resistance of 0.2–0.5 Ω sq^{-1} with 85–87% transmittance.

Besides the sheet resistance and optical transmittance, flexibility is another key factor to evaluate the performance of flexible TEs.[165,166] As mentioned in Section 2.1.1, the flexible TEs based on TCOs present insufficient flexibility due to their fragile nature. The flexible TEs based on MMNAs become potential candidates as conductive substrates in flexible electronics.[167,168] The flexibility of TEs is mostly related to three aspects: (1) the flexibility of substrates,[31,166,169] (2) the flexibility of conductive materials,[170] and (3) the adhesion between conductive materials and substrates.[171,172] The flexible substrates including flexible glass and polymer thin films should possess both high optical transmittance and flexibility. Ultrathin glass substrates present high optical transmittance, strong temperature tolerance, and excellent barriers for oxygen and humidity.[169,173] However, the low flexibility and high cost make the flexible glass less competitive than polymer substrates. In contrast, polymer substrates, such as PET, PEN, polyimide (PI), and polycarbonate (PC), present satisfactory flexibility and production cost, but lower process temperature and easier oxygen permeability.[32,166,174,175] The flexibility of MMNAs depends on the welding between junctions or the stacking of nanoparticles. More compact stacking usually leads to structures with high mechanical strength. Strong adhesion between conductive materials and substrates can prevent the exfoliation of the conductive materials, *i.e.* better flexibility. To enhance the adhesion, a variety of methods like embossed structures,[65,82] capping layers,[176] and adhesive additives[155] can be adopted. Besides the adhesion, the thickness of TEs should also be

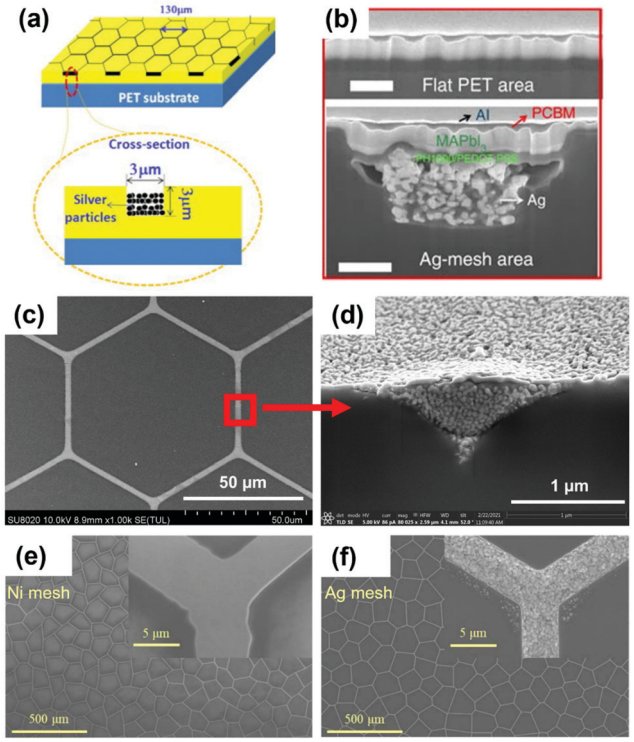

Fig. 4 (a) Schematic illustration of Ag-grid embedded in a PET substrate. Reproduced with permission from ref. 121. Copyright©2013, Elsevier B.V. (b) Cross-section SEM image of PSC based on a PET/Ag-grid/PH1000 electrode. Reproduced with permission from ref. 68 under the Creative Commons License (CC BY 4.0). (c) Top view and (d) cross-section view of embossed flexible Ag grids. Reproduced with permission from ref. 82. Copyright©2021, Elsevier B.V. SEM images of (e) Ni grids and (f) Ag grids. Reproduced with permission from ref. 65. Copyright©2020, Wiley-VCH GmbH.

considered. Thicker electrodes will generate higher stress on both surfaces under bending states.

3. Flexible PSCs based on MMNA electrodes

Fig. 5 displays three typical structures of perovskite solar cells. In inverted p–i–n structures and conventional n–i–p structures (Fig. 5a and b), transparent MMNA electrodes served as flexible anodes and cathodes, respectively, instead of ITO or FTO. For the semi-transparent structures shown in Fig. 5c, transparent MMNA electrodes were usually deposited on the top of the devices. Different device configurations require TEs with specific performance. In the following part, we will discuss the application of transparent MMNA electrodes in different PSC device configurations.

3.1. Inverted PSCs

In inverted structures, transparent MMNA electrodes are usually composited with conductive PEDOT:PSS to get a smooth surface for the fabrication of the following thin-film devices.[65,66,68,177] As shown in Fig. 6a, whether embedded or not, the surface roughness of Ag grids was reduced after coating with PEDOT:PSS.[178] The root mean square (RMS) of surface roughness decreased from 9.6 to 2.5 nm for unembedded Ag grids, while the RMS of embedded Ag grids decreased from 1.0 to 0.4 nm. The smooth surface of the transparent electrode prevented the current leakage and shortage in the thin-film devices. Similarly, Li *et al.* also coated high-conductive PEDOT:PSS on the top of the intaglio Ag mesh to decrease the surface roughness of the Ag mesh electrodes (shown in Fig. 6b).[68] However, as shown in Fig. 6c, PEDOT:PSS will lower the optical transmittance in the near-infrared region, which will decrease the J_{SC} of the solar cells. The PSCs based on PET/Ag mesh/PEDOT:PSS electrodes present a PCE of 14% with a steady-state photocurrent of 17.1 mA cm^{-2} at the maximum power point. To pursue lower sheet resistance and further boost the PCE of PSCs, Wang *et al.* adopted the Ni mesh instead of the widely used Ag mesh in TEs.[65] As mentioned before, Ni can form mesh with more compact deposition than Ag, which leads to a lower sheet resistance of the TEs. The device configuration of an inverted PSC based on this electrode is shown in Fig. 6d, where Ni-mesh/PH1000, PEDOT:PSS-NiO_x, and phenyl-C61-butyric acid methylester (PC61BM) served as a transparent anode, hole transport layer (HTL), and electron transport layer (ETL), respectively. The corresponding PSCs based on Ni mesh electrodes achieved a PCE of 17.3% with a J_{SC} of 21.78 mA cm^{-2}, a V_{OC} of 1.02 V, and an FF of 0.78 as shown in Fig. 6e. In Fig. 6f,

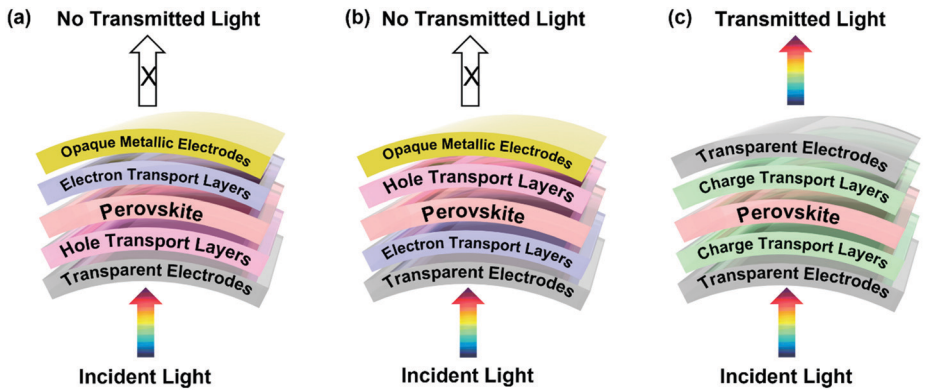

Fig. 5 Schematic device configurations of PSCs. (a) p–i–n inverted configuration. (b) n–i–p conventional configuration. (c) Semi-transparent configuration.

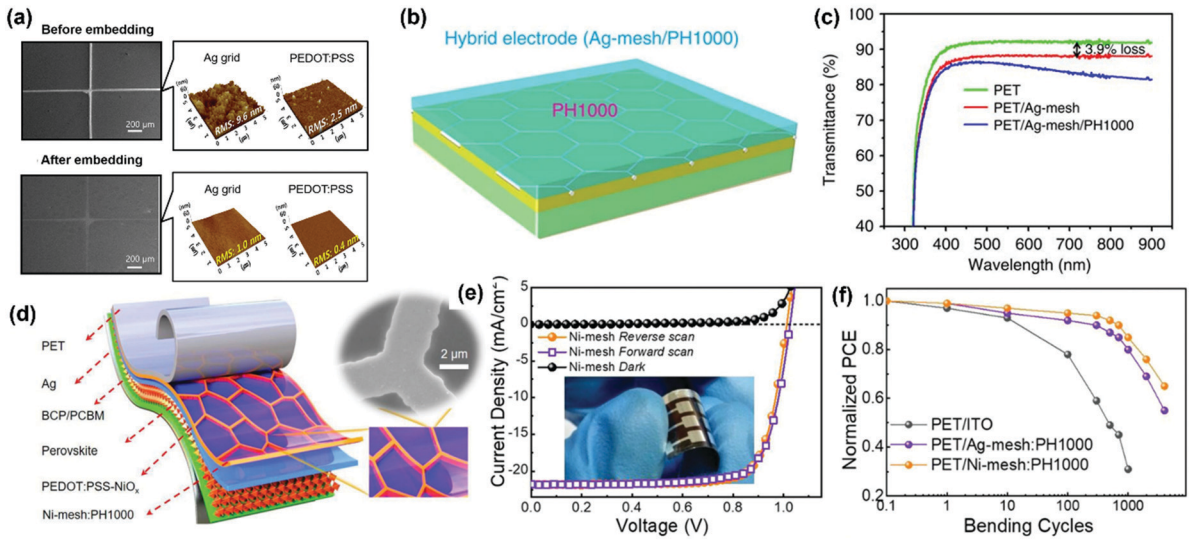

Fig. 6 (a) SEM and AFM images of Ag grids. Reproduced with permission from ref. 178 under the Creative Commons License (CC BY 4.0). (b) Schematic illustration of Ag-mesh/PH1000 electrodes. (c) Optical transmittance of PET/Ag-mesh/PH1000, PET/Ag-mesh, and PET. Reproduced with permission from ref. 68 under the Creative Commons License (CC BY 4.0). (d) Device configuration, (e) *J*–*V* characteristics, (f) mechanical stability of PSCs based on Ni-mesh electrodes. Reproduced with permission from ref. 65. Copyright©2020, Wiley-VCH GmbH.

Table 1 Summary of previously reported inverted PSCs based on MMNA electrodes

Device structure	V_{OC} (V)	J_{SC} (mA cm^{-2})	FF (%)	PCE (%)	Ref.
Glass/CuNW/PEDOT:PSS/PVK/PCBM/Bphen/Ag	0.88	9.54	58	5.10	69
PLA/AgNW/PH1000/PEDOT:PSS/PVK/PCBM/PEI/Ag	0.91	18.79	67	11.44	61
PET/c-ITO/AgNW/PEDOT:PSS/PVK/PCBM/BCP/Ag	0.99	21.53	66	14.15	179
PET/c-ITO/CuNW/PEDOT:PSS/PVK/PCBM/BCP/Ag	0.97	20.09	66	12.95	179
PTFE/graphene/AgNW/MoO_3/PVK/PCBM/BCP/Ag	0.93	17.21	65	10.42	180
PEN/AgNW/PH1000/PEDOT:PSS/PVK/PCBM/Al	0.95	18.88	69	12.85	177
PET/AgNW/m-FCE/PEDOT:PSS/PVK/PCBM/Al	1.00	18.10	74	13.32	181
PI/Cu grid/GO/PEDOT:PSS/PVK/PCBM/ZnO/Ag	0.99	21.7	76	16.4	66
PET/Ag-grid/GO/PEDOT:PSS/PVK/PFN-P1/PCBM/Ag	0.94	12.73	66	7.92	59
PET/Ni-mesh/PH1000/PEDOT:PSS-NiO_x/PVK/PCBM/BCP/Ag	1.02	21.78	78	17.3	65
PET/Cu-mesh/PH1000/Cu:NiO_x/PVK/PCBM/BCP/Cu	1.03	17.79	74	13.58	182
PET/Ag-grid/PH1000/PEDOT:PSS/PVK/PCBM/PEI/Ag	0.47	12.09	55	3.13	47
PET/Ag-mesh/PH1000/PEDOT:PSS/PVK/PCBM/Al	0.91	19.5	80	14.2	68
PET/Agmesh/PH1000/PTAA/PVK/PCBM/Al	1.05	22.34	77	18.1	183

the PSCs based on Ni mesh electrodes also showed a robust flexibility rather than that based on the Ag mesh. Table 1 summarizes the recent work on inverted PSCs based on MMNA electrodes.

Although MMNAs have been widely reported in inverted PSCs, there are still some issues faced, such as the corrosion and transmittance decrease from acid PEDOT:PSS, the band misalignment between Ag and most HTLs in inverted PSCs.[47,65,66,68,184] These aftermaths obstructed the further development of MMNAs as electrodes in PSCs. The existence of PEDOT:PSS in PSCs based on MMNA electrodes is one of the problems in inverted PSCs. The highly acidic PSS part will corrode the metal structure. Some dissociated metallic ions, like Ag^+ and Cu^+, can coordinate with the halogen (especially I^-).[185,186] The ion migration facilitates the decomposition of perovskite and generates large current hysteresis. Ma *et al.* fabricated flexible PSCs based on an Ag grid electrode as shown in Fig. 7a.[47] The TE was based on the widely reported PH1000 (a kind of highly conductive PEDOT:PSS)/Ag grid composite. In the X-ray photoelectron spectroscopy (XPS) spectrum shown in Fig. 7b, after coating with perovskite, a slight shift of the peaks related to Ag 3d orbitals in binding energy was observed. This result suggested that Ag might be oxidized from Ag^0 to Ag^+ and reacted with I^- from perovskite. According to the series XPS and UV-visible absorption results, they proposed possible reactions in the PSCs based on PH1000/Ag grid composite electrodes. As shown in Fig. 7c, firstly the acidic PH1000 oxidized the Ag^0 to Ag^+. Then the Ag^+ entered the perovskite precursor and reacted with I^-. The PH1000 layer facilitated the original Ag ion migration, which seriously damages the device performance of PSCs. To prevent the corrosion from PEDOT:PSS, Park *et al.* inserted a graphene interlayer between Cu grids and PEDOT:PSS layer.[66] The long-term stability of PSCs is displayed in Fig. 7d. The shelf stability in the glove box largely

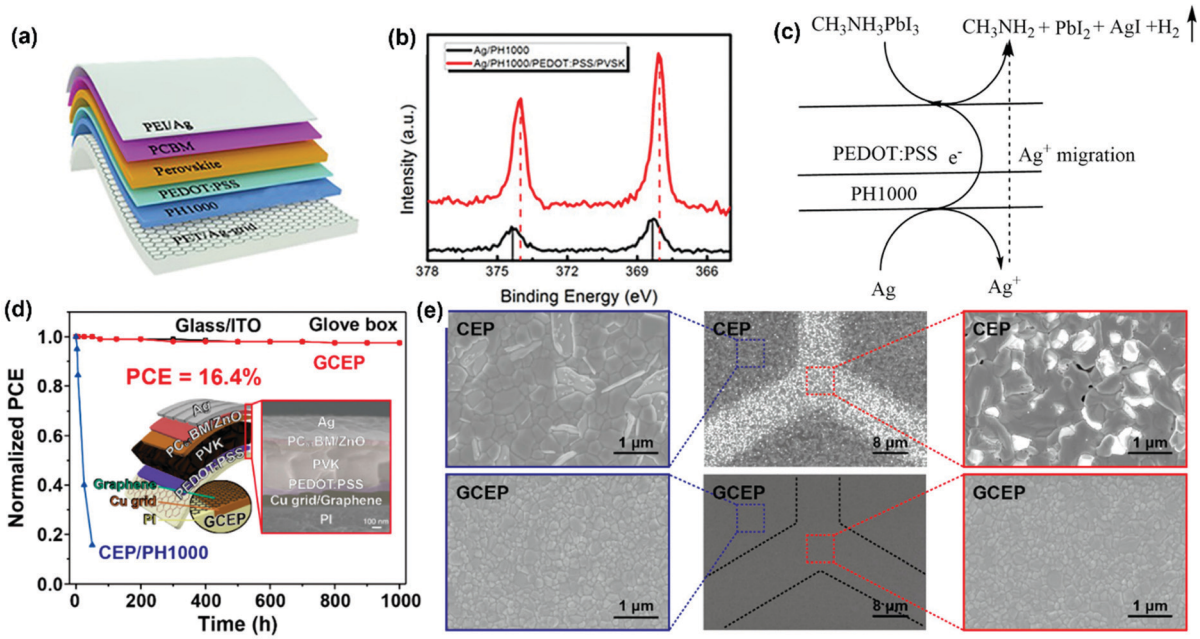

Fig. 7 (a) Device configuration of inverted PSCs based on PH1000/Ag grid anodes. (b) XPS profile of Ag 3d. (c) Proposed mechanism of Ag^+ migration. Reproduced with permission from ref. 47. Copyright©2018, Wiley-VCH GmbH. (d) Long-term stability of inverted PSCs with graphene capping layer. (e) SEM images of perovskite with/without a graphene capping layer after thermal annealing at 80 °C for 36 h. Reproduced with permission from ref. 66. Copyright©2020, American Chemical Society.

increased after inserting the graphene interlayer between PEDOT:PSS and Cu grids. After annealing at 80 °C for 36 h, the perovskite thin films with a graphene capping layer did not present any significant change compared to the serious decomposition in perovskite without a capping layer (Fig. 7e). Due to the suppression of ion migration, the corresponding PSCs reached a PCE of 16.4%. Unfortunately, after passivating the corrosion from PEDOT:PSS, most of the reported inverted PSCs based on MMNAs still possesses low V_{OC} in the region from 0.9 to 1.05 V. The low V_{OC} can be attributed to the fact that both Ag and Cu have a work function of around 4.6 eV (measured by the photoelectric effect) which is higher than the highest occupied molecular orbital (HOMO) energy levels of most HTLs in inverted PSCs.[184] For example, the most widely used PEDOT:PSS possesses a HOMO of around −5.1 to 5.2 eV.[187,188] The band misalignment between the HTL and TE is responsible for the low of V_{OC} PSCs.

3.2. Conventional PSCs

In conventional PSCs, the TEs directly contact with the ETLs. The lowest unoccupied molecular orbital (LUMO) energy levels of ETLs, such as −4.31 eV of SnO_2,[189] provide more matched band alignment in PSCs. In addition, the rid of PEDOT:PSS provides higher stability of the PSCs. On the other hand, the absence of PEDOT:PSS requires a more smooth surface of the MMNA electrodes. In most random MMNAs, especially for AgNWs, the aggregation of AgNWs causes large surface roughness, which has to combine with PEDOT:PSS to decrease the surface roughness. To address this issue, Lin *et al.* developed the orthogonal AgNWs with uniform distribution by meniscus-assisted solution printing as shown in Fig. 8a.[31] The cross-aligned AgNWs were further embossed into polymer substrates with the assistance of a ZnO layer. The AgNWs were coated on the ZnO layer. Then the pre-polymer solution was coated on AgNWs. After the pre-polymer was cured, the ZnO layer was washed with citric acid to get embedded AgNW electrodes. The transparent electrodes presented an average surface roughness of around 2.77 nm. Additionally, as displayed in Fig. 8b, the protrusion of the underlying AgNWs can slow down the evaporation of perovskite precursors leading to large-sized grains. The corresponding PSCs reached a PCE of 17.51% with an enhanced FF (Fig. 8c) compared to PSCs based on ITO/PET electrodes (16.86% shown in Fig. 8d). Song *et al.* adopted poly(methyl methacrylate) as the sacrificial layer with a similar process to embedded self-assembling Ag grids into PDMS.[82] The embossed Ag grids present a height of 70 nm, which can be inserted into the perovskite layer serving as localized electron pathways (Fig. 8f). According to the time-resolved photoluminescence (TRPL) profile presented in Fig. 8g, the TRPL lifetime decreased with the increase of the density of Ag grids, which indicates more efficient charge extraction. The PSCs based on the embossed Ag grid electrodes achieved a PCE of 18.49% with a high V_{OC} of 1.11 V. Compared to inverted PSCs, the conventional PSCs based on MMNA electrodes present higher V_{OC} and corresponding PCE due to the appropriate interface between electrodes and charge transfer layers. Table 2 summarizes the recent work on conventional PSCs based on MMNA electrodes.

3.3. Semi-transparent PSCs

Semi-transparent solar cells possess both transparent cathodes and anodes to accomplish the building-integrating requirement,

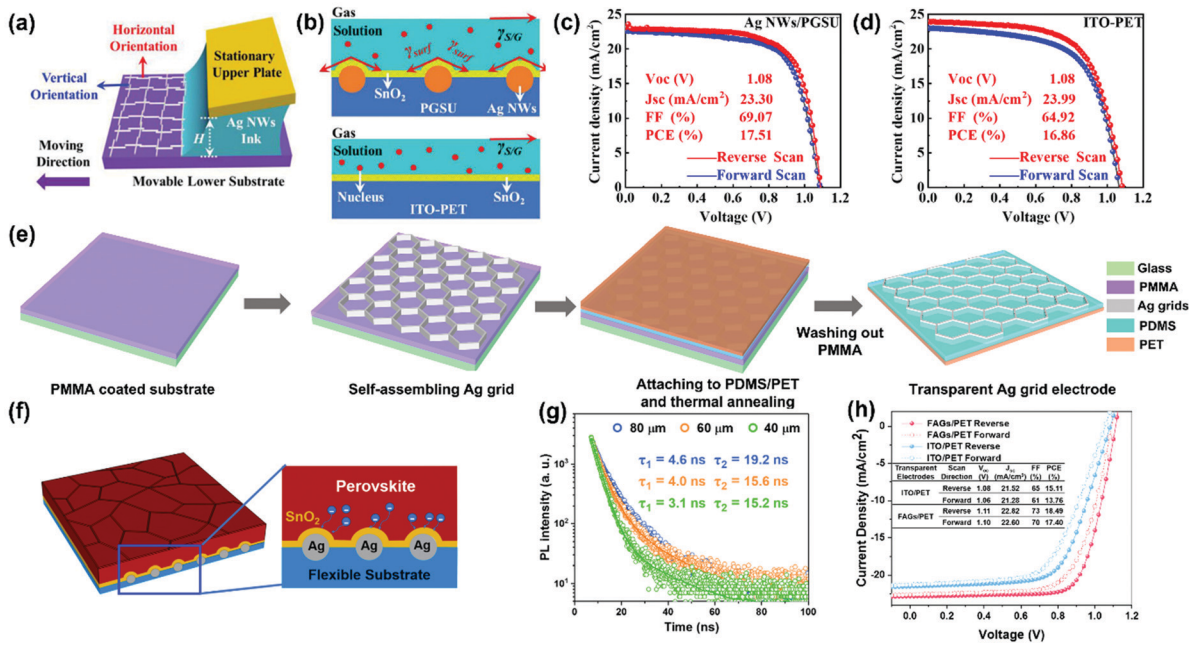

Fig. 8 (a) Schematic of the formation of cross-aligned AgNWs during the MASP process. (b) Schematic illustration of perovskite precursor solution on ITO/PET and PGSU/AgNW substrates. (c) *J*–*V* characteristics of PSCs based on PGSU/AgNW electrodes. (d) *J*–*V* characteristics of PSCs based on PET/ITO electrodes. Reproduced with permission from ref. 31. Copyright©2020, Wiley-VCH GmbH. (e) Schematic illustration of the fabrication process of embossed flexible Ag grids. (f) Schematic illustration of n charge carrier dynamics in perovskite thin films fabricated on the Ag grid electrodes. (g) TRPL intensity of perovskite thin films fabricated on Ag grid electrodes with different side lengths. (h) *J*–*V* characteristics of flexible PSCs based on Ag grid electrodes. Reproduced with permission from ref. 82. Copyright©2021, Elsevier B.V.

such as solar windows,[192] solar roofs,[193,194] and smart windscreens.[195] As for the transparent top electrodes in semi-transparent PSCs, the surface roughness of the electrode is less important than that as bottom electrodes. To replace the non-transparent light-reflecting metal top electrodes, optical transmittance and sheet resistance should be concerned as priorities. To satisfy the requirement of smart windows, the average visible transmittance (AVT) of semi-transparent PSCs should accomplish around 20% to 30% in the visible region from 400 to 700 nm.[196] The AVT is the joint result from every layer in the device. A higher transmittance of electrodes can match with thicker photo-active layers, which is beneficial to achieve higher device performance. Due to the low sheet resistance and tunable transmittance, solution-processed MMNA electrodes are regarded as a potential candidate as top electrodes in semi-transparent PSCs.[120,197–199] Brabec *et al.* fabricated semi-transparent PSCs with solution-processed AgNWs as top electrodes.[197] The device configuration is shown in Fig. 9a. A ZnO interlayer was inserted between PC61BM and AgNWs to prevent damage on lower layers during the solution process of AgNWs. The insertion of the ZnO layer also provided more appropriate band alignment between PC61BM and AgNWs, leading to higher V_{OC} and J_{SC} of PSCs. As shown in Fig. 9b, in the external quantum efficiency (EQE) spectrum, the PSCs with solution-processed AgNW top electrodes presented only around 10% lower EQE compared to that using thermally evaporated opaque Ag electrodes. The decrease in EQE is attributed to the higher sheet resistance of solution-processed AgNWs compared to thermally evaporated Ag electrodes. Overall, the semi-transparent PSCs achieved a PCE of 8.5% and an AVT of 28.4% (Fig. 9c and d). After fabricating the AgNW top electrodes, the AVT of the semi-transparent PSCs showed a negligible decrease, which is due to the high transmittance of AgNWs. Hu *et al.* reported AgNW electrodes with both high transmittance (88.4%) and hazy (13.3%).[120] The FoM value of these transparent electrodes reached 741 by using electrochemical etching methods to tailor the aspect ratio of AgNWs. The device configuration is presented in Fig. 9e, and the hazy AgNW TEs were embedded into polydimethylsiloxane and laminated on the lower PSCs. After electrochemical etching, the PVP coated on the surface of AgNWs was removed, which enhances the charge transport from the HTL to electrodes (Fig. 9f). An AVT of 9% is shown in Fig. 9g with a perovskite thickness of around 300 nm. The thicker perovskite layer leads to

Table 2 Summary of previously reported conventional PSCs based on MMNA electrodes

Device structure	V_{OC} (V)	J_{SC} (mA cm^{-2})	FF (%)	PCE (%)	Ref.
PES/AZO/AgNW/α-AZO/ZnO/PVK/spiro-OMeTAD/Au	0.99	18.9	60	11.23	190
PSGU/AgNW/SnO_2/PVK/spiro-OMeTAD/Ag	1.08	23.30	69	17.51	31
PET/Ag-grid/SnO_2/PVK/PEAI/spiro-OMeTAD/Au	1.11	22.82	73	18.49	82
PET/AgNW/F-ZnO/TiO_2/PVK/spiro-OMeTAD/Ag	0.68	12.2	40	3.29	191

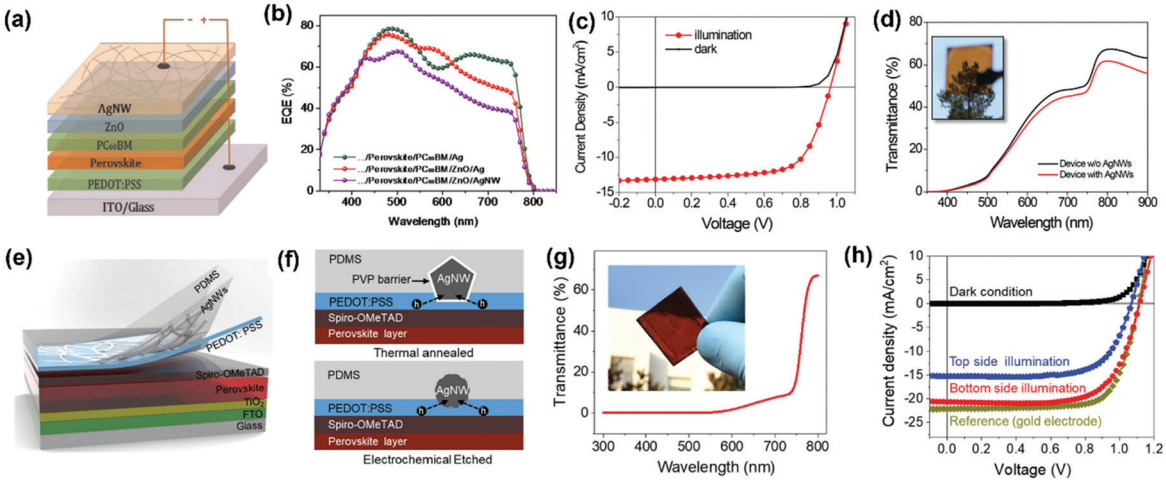

Fig. 9 (a) Device configuration, (b) EQE, (c) *J*–*V* characteristics, and (d) transmittance of semi-transmittance PSCs. Reproduced with permission from ref. 197. Copyright©2015, Royal Society of Chemistry. (e) Device configuration, (f) cross-sectional schematic of carrier transport behaviors (g) transmittance, and (h) *J*–*V* characteristics of semi-transmittance PSCs based on electrochemical etched AgNW electrodes. Reproduced with permission from ref. 120. Copyright©2018, Wiley-VCH GmbH.

Table 3 Summary of previously reported semi-transparent PSCs based on MMNA electrodes

Device structure	AVT (%)	PCE (%) (bottom incident)	PCE (%) (top incident)	Ref.
Glass/ITO/PEDOT:PSS/PSS/PVK/PCBM/PEI/AgNW	21.2	14.17	12.05	74
Glass/ITO/PTAA:F4-TCNQ/PVK/PCBM/Ag@AuNW	—	11.0	—	138
Glass/ITO/PEDOT:PSS/PSS/PVK/PCBM/PEI/AgNW	22.1	11.3	10.45	60
Glass/FTO/TiO_2/PVK/spiro-OMeTAD/PEDOT:PSS/AgNW	9	16.03	11.12	120
Glass/FTO/TiO_2/PVK/spiro-OMeTAD/Au/AgNW	—	11.07	6.10	198
Glass/FTO/TiO_2/PVK/spiro-OMeTAD/CuNW	—	9.88	—	199

a higher PCE of 16.03% illuminated from the FTO side and 11.12% illuminated from the AgNW side (shown in Fig. 9h). Table 3 summarizes the recent work on semi-transparent PSCs based on MMNA electrodes.

4. Conclusions and outlook

In this review, we highlight recent progress in transparent electrodes based on MMNAs and their applications in PSCs. The rapid development of solution-processed MMNA electrodes in PSCs makes MMNAs a potential alternative for the matured ITO electrodes. The sheet resistance and optical transmittance of the state-of-the-art MMNA electrode have already reached, even exceeded, those of commercial ITO or FTO electrodes.[32] However, there are still some challenges, such as large surface roughness, inhomogeneous deposition, and band misalignment in PSCs, obstructing the way to the future. For the fabrication of MMNAs, although the printing technology can combine with high throughput R2R processing, the printed MMNAs possess inferior electrical conductivity due to the inhomogeneous distribution and loose stacking of conductive particles. Additionally, the accuracy of the MMNAs is also limited by the printing techniques. Self-assembling, electrochemical deposition, and laser direct-writing methods can lead to compact MMNAs with high-resolution and low sheet resistance, while these methods usually are not compatible with high throughput R2R processing. What's more, the after-treatments, such as conducting polymer coating, hot substrate printing, and polymer embedding, to decrease the surface roughness usually increase the sheet resistance. In this way, developing the methods to fabricate high-quality MMNAs with a smooth surface on a large scale is urgently needed to boost the application of MMNAs as TEs in thin-film devices. For the PSCs based on MMNA electrodes, the corrosion from PEDOT:PSS, band misalignment, and ion migration restrain the further increase of PCE. Investigating suitable capping layers to suppress the corrosion from PEDOT:PSS and metallic ion migration is indispensable to improve the device performance of PSCs based on MMNA electrodes. Using highly ordered MMNA arrays to build localized charge transport channels is promising to accomplish better charge extraction and transportation, which leads to higher PCE of PSCs.

Conflicts of interest

The authors declare no conflict of interest.

Acknowledgements

The authors are grateful for the financial support from the National Natural Science Foundation of China (Grant No. 52003276,

22175185, 52003273, 51803217, 51773206, 91963212, 51961145102 and 22002171), the National Key R&D Program of China (Grant No. 2018YFA0703200 and 2018YFA0208501), the Beijing National Laboratory for Molecular Sciences (No. BNLMS-CXXM-202005 and 2019BMS20003), K. C. Wong Education Foundation, the China Postdoctoral Science Foundation (Grant No. 2020M670466), and the External Cooperation Program of Chinese Academy of Sciences (Grant No. GJHZ201948).

References

1 A. Kojima, K. Teshima, Y. Shirai and T. Miyasaka, *J. Am. Chem. Soc.*, 2009, **131**, 6050–6051.
2 https://www.nrel.gov/pv/assets/pdfs/best-research-cell-efficiencies.20200104.pdf.
3 J. Jeong, M. Kim, J. Seo, H. Lu, P. Ahlawat, A. Mishra, Y. Yang, M. A. Hope, F. T. Eickemeyer, M. Kim, Y. J. Yoon, I. W. Choi, B. P. Darwich, S. J. Choi, Y. Jo, J. H. Lee, B. Walker, S. M. Zakeeruddin, L. Emsley, U. Rothlisberger, A. Hagfeldt, D. S. Kim, M. Grätzel and J. Y. Kim, *Nature*, 2021, **592**, 381–385.
4 K. Xiao, R. X. Lin, Q. L. Han, Y. Hou, Z. Y. Qin, H. T. Nguyen, J. Wen, M. Y. Wei, V. Yeddu, M. I. Saidaminov, Y. Gao, X. Luo, Y. R. Wang, H. Gao, C. F. Zhang, J. Xu, J. Zhu, E. H. Sargent and H. R. Tan, *Nat. Energy*, 2020, **5**, 870–880.
5 T. Bu, J. Li, H. Li, C. Tian, J. Su, G. Tong, L. K. Ono, C. Wang, Z. Lin, N. Chai, X.-L. Zhang, J. Chang, J. Lu, J. Zhong, W. Huang, Y. Qi, Y.-B. Cheng and F. Huang, *Science*, 2021, **372**, 1327.
6 J. Peng, D. Walter, Y. H. Ren, M. Tebyetekerwa, Y. L. Wu, T. Duong, Q. L. Lin, J. T. Li, T. Lu, M. A. Mahmud, O. L. C. Lem, S. Y. Zhao, W. Z. Liu, Y. Liu, H. P. Shen, L. Li, F. Kremer, H. T. Nguyen, D. Y. Choi, K. J. Weber, K. R. Catchpole and T. P. White, *Science*, 2021, **371**, 390.
7 T. Zhu and X. Gong, *InfoMat*, 2021, **3**, 1039–1069.
8 Y. Lei, Y. Chen, R. Zhang, Y. Li, Q. Yan, S. Lee, Y. Yu, H. Tsai, W. Choi, K. Wang, Y. Luo, Y. Gu, X. Zheng, C. Wang, C. Wang, H. Hu, Y. Li, B. Qi, M. Lin, Z. Zhang, S. A. Dayeh, M. Pharr, D. P. Fenning, Y. H. Lo, J. Luo, K. Yang, J. Yoo, W. Nie and S. Xu, *Nature*, 2020, **583**, 790–795.
9 D. Yang, R. Yang, S. Priya and S. F. Liu, *Angew. Chem., Int. Ed.*, 2019, **58**, 4466–4483.
10 X. Hu, X. Meng, L. Zhang, Y. Zhang, Z. Cai, Z. Huang, M. Su, Y. Wang, M. Li, F. Li, X. Yao, F. Wang, W. Ma, Y. Chen and Y. Song, *Joule*, 2019, **3**, 2205–2218.
11 L. Hu, Q. Zhao, S. Huang, J. Zheng, X. Guan, R. Patterson, J. Kim, L. Shi, C. H. Lin, Q. Lei, D. Chu, W. Tao, S. Cheong, R. D. Tilley, A. W. Y. Ho-Baillie, J. M. Luther, J. Yuan and T. Wu, *Nat. Commun.*, 2021, **12**, 466.
12 X. T. Hu, Z. Q. Huang, X. Zhou, P. W. Li, Y. Wang, Z. D. Huang, M. Su, W. J. Ren, F. Y. Li, M. Z. Li, Y. W. Chen and Y. L. Song, *Adv. Mater.*, 2017, **29**, 1703236.
13 L. Wang, Y. X. Xue, M. H. Cui, Y. M. Huang, H. Y. Xu, C. C. Qin, J. Yang, H. T. Dai and M. J. Yuan, *Angew. Chem., Int. Ed.*, 2020, **59**, 6442–6450.
14 M. Wang, H. X. Sun, F. R. Cao, W. Tian and L. Li, *Adv. Mater.*, 2021, **33**, 2100625.
15 S. F. Leung, K. T. Ho, P. K. Kung, V. K. S. Hsiao, H. N. Alshareef, Z. L. Wang and J. H. He, *Adv. Mater.*, 2018, **30**, 1704611.
16 K. Shen, H. Xu, X. Li, J. Guo, S. Sathasivam, M. Q. Wang, A. B. Ren, K. L. Choy, I. P. Parkin, Z. X. Guo and J. Wu, *Adv. Mater.*, 2020, **32**, 2000004.
17 Y. Shen, M. N. Li, Y. Q. Li, F. M. Xie, H. Y. Wu, G. H. Zhang, L. Chen, S. T. Lee and J. X. Tang, *ACS Nano*, 2020, **14**, 6107–6116.
18 H. K. Seo, H. Kim, J. Lee, M. H. Park, S. H. Jeong, Y. H. Kim, S. J. Kwon, T. H. Han, S. Yoo and T. W. Lee, *Adv. Mater.*, 2017, **29**, 1605587.
19 H. Kim, H. N. Ra, J. S. Kim, S. H. Paek, J. Park and Y. C. Kim, *J. Ind. Eng. Chem.*, 2020, **90**, 117–121.
20 F. C. Zhao, D. Chen, S. Chang, H. L. Huang, K. Tong, C. T. Xiao, S. Y. Chou, H. Z. Zhong and Q. B. Pei, *J. Mater. Chem. C*, 2017, **5**, 531–538.
21 Z. H. Yu, Z. B. Yang, Z. Y. Ni, Y. C. Shao, B. Chen, Y. Z. Lin, H. T. Wei, Z. S. J. Yu, Z. Holman and J. S. Huang, *Nat. Energy*, 2020, **5**, 657–665.
22 K. Wang, C. Wu, Y. Hou, D. Yang, T. Ye, J. Yoon, M. Sanghadasa and S. Priya, *Energy Environ. Sci.*, 2020, **13**, 3412–3422.
23 S. Bai, P. M. Da, C. Li, Z. P. Wang, Z. C. Yuan, F. Fu, M. Kawecki, X. J. Liu, N. Sakai, J. T. W. Wang, S. Huettner, S. Buecheler, M. Fahlman, F. Gao and H. J. Snaith, *Nature*, 2019, **571**, 245.
24 G. Kim, H. Min, K. S. Lee, D. Y. Lee, S. M. Yoon and S. I. Seok, *Science*, 2020, **370**, 108.
25 A. F. Palmstrom, G. E. Eperon, T. Leijtens, R. Prasanna, S. N. Habisreutinger, W. Nemeth, E. A. Gaulding, S. P. Dunfield, M. Reese, S. Nanayakkara, T. Moot, J. Werner, J. Liu, B. To, S. T. Christensen, M. D. McGehee, M. F. A. M. van Hest, J. M. Luther, J. J. Berry and D. T. Moore, *Joule*, 2019, **3**, 2193–2204.
26 J. Chung, S. S. Shin, K. Hwang, G. Kim, K. W. Kim, D. S. Lee, W. Kim, B. S. Ma, Y.-K. Kim, T.-S. Kim and J. Seo, *Energy Environ. Sci.*, 2020, **13**, 4854–4861.
27 S. A. Hashemi, S. Ramakrishna and A. G. Aberle, *Energy Environ. Sci.*, 2020, **13**, 685–743.
28 X. Hu, Z. Huang, F. Li, M. Su, Z. Huang, Z. Zhao, Z. Cai, X. Yang, X. Meng, P. Li, Y. Wang, M. Li, Y. Chen and Y. Song, *Energy Environ. Sci.*, 2019, **12**, 979–987.
29 X. Hu, F. Li and Y. Song, *ACS Energy Lett.*, 2019, **4**, 1065–1072.
30 X. C. Meng, Z. Xing, X. T. Hu, Z. Q. Huang, T. Hu, L. C. Tan, F. Y. Li and Y. W. Chen, *Angew. Chem., Int. Ed.*, 2020, **59**, 16602–16608.
31 J. Qi, S. Chen, C. Lan, A. C. Wang, X. Cui, Z. You, Q. Zhang, Y. Li, Z. L. Wang, H. Wang and Z. Lin, *Adv. Energy Mater.*, 2020, **10**, 2001185.
32 Y. Zhang, S. W. Ng, X. Lu and Z. Zheng, *Chem. Rev.*, 2020, **120**, 2049–2122.
33 N. G. Park, *Adv. Energy Mater.*, 2020, **10**, 1903106.

34 V. Zardetto, T. M. Brown, A. Reale and A. Di Carlo, *J. Polym. Sci., Part B: Polym. Phys.*, 2011, **49**, 638–648.
35 J. Ahn, H. Hwang, S. Jeong and J. Moon, *Adv. Energy Mater.*, 2017, **7**, 1602751.
36 M. R. Azani, A. Hassanpour and T. Torres, *Adv. Energy Mater.*, 2020, **10**, 2002536.
37 C. X. Bao, W. D. Zhu, J. Yang, F. M. Li, S. Gu, Y. R. Q. Wang, T. Yu, J. Zhu, Y. Zhou and Z. G. Zou, *ACS Appl. Mater. Interfaces*, 2016, **8**, 23868–23875.
38 H. Kang, Y. Kim, S. Cheon, G. R. Yi and J. H. Cho, *ACS Appl. Mater. Interfaces*, 2017, **9**, 30779–30785.
39 R. R. da Silva, M. X. Yang, S. I. Choi, M. F. Chi, M. Luo, C. Zhang, Z. Y. Li, P. H. C. Camargo, S. J. L. Ribeiro and Y. N. Xia, *ACS Nano*, 2016, **10**, 7892–7900.
40 Z. Jiang, K. Fukuda, X. Xu, S. Park, D. Inoue, H. Jin, M. Saito, I. Osaka, K. Takimiya and T. Someya, *Adv. Mater.*, 2018, **30**, 1707526.
41 E. Lee, J. Ahn, H. C. Kwon, S. Ma, K. Kim, S. Yun and J. Moon, *Adv. Energy Mater.*, 2018, **8**, 1702182.
42 J. Schneider, P. Rohner, D. Thureja, M. Schmid, P. Galliker and D. Poulikakos, *Adv. Funct. Mater.*, 2016, **26**, 833–840.
43 Z. Jiang, K. Fukuda, X. M. Xu, S. Park, D. Inoue, H. Jin, M. Saito, I. Osaka, K. Takimiya and T. Someya, *Adv. Mater.*, 2018, **30**, 1707526.
44 Y. N. Sun, M. J. Chang, L. X. Meng, X. J. Wan, H. H. Gao, Y. M. Zhang, K. Zhao, Z. H. Sun, C. X. Li, S. R. Liu, H. K. Wang, J. J. Liang and Y. S. Chen, *Nat. Electron.*, 2019, **2**, 513–520.
45 W. K. Kim, S. Lee, D. Hee Lee, I. Hee Park, J. Seong Bae, T. Woo Lee, J. Y. Kim, J. Hun Park, Y. Chan Cho, C. Ryong Cho and S. Y. Jeong, *Sci. Rep.*, 2015, **5**, 10715.
46 K.-W. Seo, Y.-J. Noh, S.-I. Na and H.-K. Kim, *Sol. Energy Mater. Sol. Cells*, 2016, **155**, 51–59.
47 J. Wang, X. Chen, F. Jiang, Q. Luo, L. Zhang, M. Tan, M. Xie, Y.-Q. Li, Y. Zhou, W. Su, Y. Li and C.-Q. Ma, *Sol. RRL*, 2018, **2**, 1800118.
48 T. Zhu, Y. R. Yang, X. Yao, Z. X. Huang, L. Liu, W. P. Hu and X. Gong, *ACS Appl. Mater. Interfaces*, 2020, **12**, 15456–15463.
49 Z. W. Jin, J. Yan, X. Huang, W. Xu, S. Y. Yang, D. B. Zhu and J. Z. Wang, *Nano Energy*, 2017, **40**, 376–381.
50 Y. Y. Jiang, B. W. Luo, F. Y. Jiang, F. B. Jiang, C. Fuentes-Hernandez, T. F. Liu, L. Mao, S. X. Xiong, Z. F. Li, T. Wang, B. Kippelen and Y. H. Zhou, *Nano Lett.*, 2016, **16**, 7829–7835.
51 B. J. Worfolk, S. C. Andrews, S. Park, J. Reinspach, N. Liu, M. F. Toney, S. C. Mannsfeld and Z. Bao, *Proc. Natl. Acad. Sci. U. S. A.*, 2015, **112**, 14138–14143.
52 Y. Wang, C. X. Zhu, R. Pfattner, H. P. Yan, L. H. Jin, S. C. Chen, F. Molina-Lopez, F. Lissel, J. Liu, N. I. Rabiah, Z. Chen, J. W. Chung, C. Linder, M. F. Toney, B. Murmann and Z. Bao, *Sci. Adv.*, 2017, **3**, e1602076.
53 D. Zhang, Y. J. Tang, Y. X. Zhang, F. Y. Yang, Y. L. Liu, X. Y. Wang, J. T. Yang, X. Gong and J. Zheng, *J. Mater. Chem. A*, 2020, **8**, 20474–20485.
54 I. Jeon, R. Xiang, A. Shawky, Y. Matsuo and S. Maruyama, *Adv. Energy Mater.*, 2019, **9**, 1801312.
55 I. Jeon, J. Yoon, U. Kim, C. Lee, R. Xiang, A. Shawky, J. Xi, J. Byeon, H. M. Lee, M. Choi, S. Maruyama and Y. Matsuo, *Adv. Energy Mater.*, 2019, **9**, 1901204.
56 Q. Luo, H. Ma, Q. Z. Hou, Y. X. Li, J. Ren, X. Z. Dai, Z. B. Yao, Y. Zhou, L. C. Xiang, H. Y. Du, H. C. He, N. Wang, K. L. Jiang, H. Lin, H. W. Zhang and Z. H. Guo, *Adv. Funct. Mater.*, 2018, **28**, 1706777.
57 Q. Luo, R. Wu, L. Ma, C. Wang, H. Liu, H. Lin, N. Wang, Y. Chen and Z. Guo, *Adv. Funct. Mater.*, 2020, **31**, 2004765.
58 I. Jeon, J. Yoon, N. Ahn, M. Atwa, C. Delacou, A. Anisimov, E. I. Kauppinen, M. Choi, S. Maruyama and Y. Matsuo, *J. Phys. Chem. Lett.*, 2017, **8**, 5395–5401.
59 H. F. Lu, J. S. Sun, H. Zhang, S. M. Lu and W. C. H. Choy, *Nanoscale*, 2016, **8**, 5946–5953.
60 K. Han, M. Xie, L. Zhang, L. Yan, J. Wei, G. Ji, Q. Luo, J. Lin, Y. Hao and C.-Q. Ma, *Sol. Energy Mater. Sol. Cells*, 2018, **185**, 399–405.
61 Z. Lu, Y. H. Lou, P. P. Ma, K. P. Zhu, S. Cong, C. Wang, X. D. Su and G. F. Zou, *Sol. RRL*, 2020, **4**, 2000320.
62 W. X. Zhang, W. Song, J. M. Huang, L. K. Huang, T. T. Yan, J. F. Ge, R. X. Peng and Z. Y. Ge, *J. Mater. Chem. A*, 2019, **7**, 22021–22028.
63 X. Gan, R. T. Lv, H. Y. Zhu, L. P. Ma, X. Y. Wang, Z. X. Zhang, Z. H. Huang, H. W. Zhu, W. C. Ren, M. Terrones and F. Y. Kang, *J. Mater. Chem. A*, 2016, **4**, 13795–13802.
64 Z. Y. Chen, R. T. Yin, S. N. Obaid, J. B. Tian, S. W. Chen, A. N. Miniovich, N. Boyajian, I. R. Efimov and L. Y. Lu, *Adv. Mater. Technol.*, 2020, **5**, 2000322.
65 M. Li, W. W. Zuo, A. G. Ricciardulli, Y. G. Yang, Y. H. Liu, Q. Wang, K. L. Wang, G. X. Li, M. Saliba, D. Di Girolamo, A. Abate and Z. K. Wang, *Adv. Mater.*, 2020, **32**, 2003422.
66 G. Jeong, D. Koo, J. Seo, S. Jung, Y. Choi, J. Lee and H. Park, *Nano Lett.*, 2020, **20**, 3718–3727.
67 Q. Sun, J. D. Chen, J. W. Zheng, T. Y. Qu, T. Y. Jin, Y. Q. Li and J. X. Tang, *Adv. Opt. Mater.*, 2019, **7**, 1900847.
68 Y. Li, L. Meng, Y. M. Yang, G. Xu, Z. Hong, Q. Chen, J. You, G. Li, Y. Yang and Y. Li, *Nat. Commun.*, 2016, **7**, 10214.
69 Q. J. Sun, X. L. Shi, X. C. Wang, Y. Y. Zhai, L. Y. Gao, Z. F. Li, Y. Y. Hao and Y. C. Wu, *Org. Electron.*, 2019, **75**, 105428.
70 J. Yang, C. X. Bao, K. Zhu, T. Yu and Q. Y. Xu, *ACS Appl. Mater. Interfaces*, 2018, **10**, 1996–2003.
71 D. Kumar, V. Stoichkov, E. Brousseau, G. C. Smith and J. Kettle, *Nanoscale*, 2019, **11**, 5771.
72 X. Liu, X. Y. Guo, Y. Lv, Y. S. Hu, J. Lin, Y. Fan, N. Zhang and X. Y. Liu, *ACS Appl. Mater. Interfaces*, 2018, **10**, 18141–18148.
73 K. P. Zhu, Z. Lu, S. Cong, G. J. Cheng, P. P. Ma, Y. H. Lou, J. N. Ding, N. Y. Yuan, M. H. Rummeli and G. F. Zou, *Small*, 2019, **15**, 1902878.
74 M. L. Xie, H. Lu, L. P. Zhang, J. Wang, Q. Luo, J. Lin, L. X. Ba, H. Liu, W. Z. Shen, L. Y. Shi and C. Q. Ma, *Sol. RRL*, 2018, **2**, 1700184.
75 J. H. Du, H. Jin, Z. K. Zhang, D. D. Zhang, S. Jia, L. P. Ma, W. C. Ren, H. M. Cheng and P. L. Burn, *Nanoscale*, 2017, **9**, 251–257.

76 A. G. Ricciardulli, S. Yang, G. J. A. H. Wetzelaer, X. L. Feng and P. W. M. Blom, *Adv. Funct. Mater.*, 2018, **28**, 1706010.
77 I. Jeon, S. Seo, Y. Sato, C. Delacou, A. Anisimov, K. Suenaga, E. I. Kauppinen, S. Maruyama and Y. Matsuo, *J. Phys. Chem. C*, 2017, **121**, 25743–25749.
78 L. Zhou, M. J. Yu, X. L. Chen, S. H. Nie, W. Y. Lai, W. Su, Z. Cui and W. Huang, *Adv. Funct. Mater.*, 2018, **28**, 1705955.
79 W. Song, X. Fan, B. G. Xu, F. Yan, H. Q. Cui, Q. Wei, R. X. Peng, L. Hong, J. M. Huang and Z. Y. Ge, *Adv. Mater.*, 2018, **30**, 1800075.
80 P. You, Z. K. Liu, Q. D. Tai, S. H. Liu and F. Yan, *Adv. Mater.*, 2015, **27**, 3632–3638.
81 J. H. Heo, D. H. Shin, D. H. Song, D. H. Kim, S. J. Lee and S. H. Im, *J. Mater. Chem. A*, 2018, **6**, 8251–8258.
82 Y. Yang, F. Min, Y. Qiao, Z. Li, F. Vogelbacher, Z. Liu, W. Lv, Y. Wang and Y. Song, *Nano Energy*, 2021, **89**, 106384.
83 H. D. Um, D. Choi, A. Choi, J. H. Seo and K. Seo, *ACS Nano*, 2017, **11**, 6218–6224.
84 S. Z. Oener, J. van de Groep, B. Macco, P. C. P. Bronsveld, W. M. M. Kessels, A. Polman and E. C. Garnett, *Nano Lett.*, 2016, **16**, 3689–3695.
85 C. P. Muzzillo, E. Wong, L. M. Mansfield, J. Simon and A. J. Ptak, *ACS Appl. Mater. Interfaces*, 2020, **12**, 41471–41476.
86 P. Y. Huo, I. Lombardero, I. Garcia and I. Rey-Stolle, *Prog. Photovoltaics*, 2019, **27**, 789–797.
87 C. P. Muzzillo, M. O. Reese and L. M. Mansfield, *ACS Appl. Mater. Interfaces*, 2020, **12**, 25895–25902.
88 A. Kim, Y. Won, K. Woo, S. Jeong and J. Moon, *Adv. Funct. Mater.*, 2014, **24**, 2462–2471.
89 F. Tsin, J. Rousset, A. Le Bris and D. Lincot, *Prog. Photovoltaics*, 2016, **24**, 1123–1132.
90 X. Wang, R. R. Wang, H. T. Zhai, L. J. Shi and J. Sun, *J. Mater. Chem. C*, 2018, **6**, 5738–5745.
91 J. Wu, X. L. Que, Q. Hu, D. Y. Luo, T. H. Liu, F. Liu, T. P. Russell, R. Zhu and Q. H. Gong, *Adv. Funct. Mater.*, 2016, **26**, 4822–4828.
92 G. Wang, J. Zhang, C. Yang, Y. Wang, Y. Xing, M. A. Adil, Y. Yang, L. Tian, M. Su, W. Shang, K. Lu, Z. Shuai and Z. Wei, *Adv. Mater.*, 2020, **32**, 2005153.
93 S. M. Lee, H. W. Koo, T. W. Kim and H. K. Kim, *Surf. Coat. Technol.*, 2018, **343**, 115–120.
94 R. Pruna, M. Lopez and F. Teixidor, *Nanoscale*, 2019, **11**, 276–284.
95 B. Azzopardi, C. J. M. Emmott, A. Urbina, F. C. Krebs, J. Mutale and J. Nelson, *Energy Environ. Sci.*, 2011, **4**, 3741–3753.
96 S. R. Ye, A. R. Rathmell, Z. F. Chen, I. E. Stewart and B. J. Wiley, *Adv. Mater.*, 2014, **26**, 6670–6687.
97 M. Nicolescu, M. Anastasescu, J. M. Calderon-Moreno, A. V. Maraloiu, V. S. Teodorescu, S. Preda, L. Predoana, M. Zaharescu and M. Gartner, *Opt. Mater.*, 2021, **114**, 110999.
98 A. K. Chu, W. C. Tien, S. W. Lai, H. L. Tsai, R. Y. Bai, X. Z. Lin and L. Y. Chen, *Org. Electron.*, 2017, **46**, 99–104.
99 Y. J. Liu, T. Moser, C. Andres, L. Gorjan, A. Remhof, F. Clemens, T. Graule, A. N. Tiwari and Y. E. Romanyuk, *J. Mater. Chem. A*, 2019, **7**, 3083–3089.
100 T. Zhu, Y. R. Yang, L. Y. Zheng, L. Liu, M. L. Becker and X. Gong, *Adv. Funct. Mater.*, 2020, **30**, 1909487.
101 E. Dauzon, Y. B. Lin, H. Faber, E. Yengel, X. Sallenave, C. Plesse, F. Goubard, A. Amassian and T. D. Anthopoulos, *Adv. Funct. Mater.*, 2020, **30**, 2001251.
102 C. Yi, L. N. Shen, J. Zheng and X. Gong, *Sci. Rep.*, 2021, **11**, 18222.
103 G. Zeng, J. W. Zhang, X. B. Chen, H. W. Gu, Y. W. Li and Y. F. Li, *Sci. China: Chem.*, 2019, **62**, 851–858.
104 M. U. Halbich, D. Zielke, R. Gogolin, R. Sauer-Stieglitz, W. Lovenich and J. Schmidt, *Sci. Rep.*, 2019, **9**, 9775.
105 J. Q. Qin, L. K. Lan, S. S. Chen, F. N. Huang, H. R. Shi, W. J. Chen, H. B. Xia, K. Sun and C. D. Yang, *Adv. Funct. Mater.*, 2020, **30**, 2002529.
106 Z. Gao, T. Gao, Q. Geng, G. Lin, Y. Li, L. Chen and M. Li, *Sol. Energy*, 2021, **228**, 299–307.
107 B. Cho, K. S. Park, J. Baek, H. S. Oh, Y. E. K. Lee and M. M. Sung, *Nano Lett.*, 2014, **14**, 3321–3327.
108 M. N. Gueye, A. Carella, N. Massonnet, E. Yvenou, S. Brenet, J. Faure-Vincent, S. Pouget, F. Rieutord, H. Okuno, A. Benayad, R. Demadrille and J. P. Simonato, *Chem. Mater.*, 2016, **28**, 3462–3468.
109 X. Fan, W. Y. Nie, S. H. Tsai, N. X. Wang, H. H. Huang, Y. J. Cheng, R. J. Wen, L. J. Ma, F. Yan and Y. G. Xia, *Adv. Sci.*, 2019, **6**, 1900813.
110 L. Qian, Y. Xie, Y. Yu, S. S. Wang, S. C. Zhang and J. Zhang, *Angew. Chem., Int. Ed.*, 2020, **59**, 10884–10887.
111 S. C. Zhang, X. Wang, F. R. Yao, M. S. He, D. W. Lin, H. Ma, Y. Y. Sun, Q. C. Zhao, K. H. Liu, F. Ding and J. Zhang, *Chem*, 2019, **5**, 1182–1193.
112 P. X. Hou, W. S. Li, S. Y. Zhao, G. X. Li, C. Shi, C. Liu and H. M. Cheng, *ACS Nano*, 2014, **8**, 7156–7162.
113 Y. Chen, Y. Y. Yue, S. R. Wang, N. Zhang, J. Feng and H. B. Sun, *Adv. Electron. Mater.*, 2019, **5**, 1900247.
114 R. K. L. Tan, S. P. Reeves, N. Hashemi, D. G. Thomas, E. Kavak, R. Montazami and N. N. Hashemi, *J. Mater. Chem. A*, 2017, **5**, 17777–17803.
115 J. H. Heo, D. H. Shin, M. H. Jang, M. L. Lee, M. G. Kang and S. H. Im, *J. Mater. Chem. A*, 2017, **5**, 21146–21152.
116 S. Tongay, K. Berke, M. Lemaitre, Z. Nasrollahi, D. B. Tanner, A. F. Hebard and B. R. Appleton, *Nanotechnology*, 2011, **22**, 425701.
117 C. Petridis, D. Konios, M. M. Stylianakis, G. Kakavelakis, M. Sygletou, K. Savva, P. Tzourmpakis, M. Krassas, N. Vaenas, E. Stratakis and E. Kymakis, *Nanoscale Horiz.*, 2016, **1**, 375–382.
118 P. K. Jha, S. K. Singh, V. Kumar, S. Rana, S. Kurungot and N. Ballav, *Chem*, 2017, **3**, 846–860.
119 T. Araki, J. T. Jiu, M. Nogi, H. Koga, S. Nagao, T. Sugahara and K. Suganuma, *Nano Res.*, 2014, **7**, 236–245.
120 Y. Fang, Z. Wu, J. Li, F. Jiang, K. Zhang, Y. Zhang, Y. Zhou, J. Zhou and B. Hu, *Adv. Funct. Mater.*, 2018, **28**, 1705409.
121 Y. Li, L. Mao, Y. Gao, P. Zhang, C. Li, C. Ma, Y. Tu, Z. Cui and L. Chen, *Sol. Energy Mater. Sol. Cells*, 2013, **113**, 85–89.
122 C. Preston, Y. Xu, X. Han, J. N. Munday and L. Hu, *Nano Res.*, 2013, **6**, 461–468.

123 Z. Y. Chen, N. Boyajian, Z. X. Lin, R. T. Yin, S. N. Obaid, J. B. Tian, J. A. Brennan, S. W. Chen, A. N. Miniovich, L. Q. Lin, Y. R. Qi, X. T. Liu, I. R. Efimov and L. Y. Lu, *Adv. Mater. Technol.*, 2021, **6**, 2100225.
124 H. Hwang, A. Kim, Z. Zhong, H. C. Kwon, S. Jeong and J. Moon, *Adv. Funct. Mater.*, 2016, **26**, 6545–6554.
125 M. Singh and S. Rana, *Mater. Today Commun.*, 2020, **24**, 101317.
126 M. J. Kim, P. F. Flowers, I. E. Stewart, S. R. Ye, S. Baek, J. J. Kim and B. J. Wiley, *J. Am. Chem. Soc.*, 2017, **139**, 277–284.
127 Y. Lu, S. H. Yang, J. Xu, Z. Z. Liu, H. Wang, M. Lin, Y. W. Wang and H. Y. Chen, *Small*, 2018, **14**, 1801925.
128 S. N. Obaid, R. T. Yin, J. B. Tian, Z. Y. Chen, S. W. Chen, K. B. Lee, N. Boyajian, A. N. Miniovich, I. R. Efimov and L. Y. Lu, *Adv. Funct. Mater.*, 2020, **30**, 1910027.
129 Q. Shao, K. Y. Lu and X. Q. Huang, *Small Methods*, 2019, **3**, 1800545.
130 J. Kim, W. J. da Silva, A. R. B. Yusoff and J. Jang, *Sci. Rep.*, 2016, **6**, 19813.
131 T. Sannicolo, M. Lagrange, A. Cabos, C. Celle, J. P. Simonato and D. Bellet, *Small*, 2016, **12**, 6052–6075.
132 P. Y. Yi, C. P. Zhang, L. F. Peng and X. M. Lai, *RSC Adv.*, 2017, **7**, 48835–48840.
133 H. Y. Zhou, H. D. Mao, X. C. Meng, Q. X. Wang, L. C. Tan and Y. W. Chen, *Org. Electron.*, 2019, **75**, 105408.
134 Y. H. Liu, J. L. Xu, X. Gao, Y. L. Sun, J. J. Lv, S. Shen, L. S. Chen and S. D. Wang, *Energy Environ. Sci.*, 2017, **10**, 2534–2543.
135 J. Jang, H. G. Im, J. Jin, J. Lee, J. Y. Lee and B. S. Bae, *ACS Appl. Mater. Interfaces*, 2016, **8**, 27035–27043.
136 D. H. Cho, O. E. Kwon, Y. S. Park, B. G. Yu, J. Lee, J. Moon, H. Cho, H. Lee and N. S. Cho, *Org. Electron.*, 2017, **50**, 170–176.
137 G. Hassan, J. Bae and C. H. Lee, *J. Mater. Sci.: Mater. Electron.*, 2018, **29**, 49–55.
138 T. Liu, W. Q. Liu, Y. T. Zhu, S. P. Wang, G. Wu and H. Z. Chen, *Sol. Energy Mater. Sol. Cells*, 2017, **171**, 43–49.
139 X. B. Chen, G. Y. Xu, G. Zeng, H. W. Gu, H. Y. Chen, H. T. Xu, H. F. Yao, Y. W. Li, J. H. Hou and Y. F. Li, *Adv. Mater.*, 2020, **32**, 1908478.
140 J. K. Han, J. K. Yang, W. W. Gao and H. Bai, *Adv. Funct. Mater.*, 2021, **31**, 2010155.
141 F. Qin, L. L. Sun, H. T. Chen, Y. Liu, X. Lu, W. Wang, T. F. Liu, X. Y. Dong, P. Jiang, Y. Y. Jiang, L. Wang and Y. H. Zhou, *Adv. Mater.*, 2021, **33**, 2103017.
142 M. R. Azani, A. Hassanpour, Y. Y. Tarasevich, I. V. Vodolazskaya and A. V. Eserkepov, *J. Appl. Phys.*, 2019, **125**, 234903.
143 M. R. Azani and A. Hassanpour, *Chem. – Eur. J.*, 2018, **24**, 19195–19199.
144 M. J. Kim, S. Alvarez, Z. H. Chen, K. A. Fichthorn and B. J. Wiley, *J. Am. Chem. Soc.*, 2018, **140**, 14740–14746.
145 Y. G. Sun, B. Gates, B. Mayers and Y. N. Xia, *Nano Lett.*, 2002, **2**, 165–168.
146 Y. G. Sun, B. Mayers, T. Herricks and Y. N. Xia, *Nano Lett.*, 2003, **3**, 955–960.
147 R. Zhu, C. H. Chung, K. C. Cha, W. B. Yang, Y. B. Zheng, H. P. Zhou, T. B. Song, C. C. Chen, P. S. Weiss, G. Li and Y. Yang, *ACS Nano*, 2011, **5**, 9877–9882.
148 Y. J. Shiau, K. M. Chiang and H. W. Lin, *Nanoscale*, 2015, **7**, 12698–12705.
149 T. Sannicolo, N. Charvin, L. Flandin, S. Kraus, D. T. Papanastasiou, C. Celle, J. P. Simonato, D. Munoz-Rojas, C. Jimenez and D. Bellet, *ACS Nano*, 2018, **12**, 4648–4659.
150 W. H. Chung, S. H. Park, S. J. Joo and H. S. Kim, *Nano Res.*, 2018, **11**, 2190–2203.
151 J. Kim, Y. S. Nam, M. H. Song and H. W. Park, *ACS Appl. Mater. Interfaces*, 2016, **8**, 20938–20945.
152 H. F. Lu, D. Zhang, J. Q. Cheng, J. Liu, J. Mao and W. C. H. Choy, *Adv. Funct. Mater.*, 2015, **25**, 4211–4218.
153 C. Wang, B. S. Cheng, H. C. Zhang, P. B. Wan, L. Luo, Y. Kuang and X. M. Sun, *Nano Res.*, 2016, **9**, 1532–1542.
154 Y. Zhang, J. N. Guo, D. Xu, Y. Sun and F. Yan, *ACS Appl. Mater. Interfaces*, 2017, **9**, 25465–25473.
155 M. Han, Y. J. Ge, J. F. Liu, Z. Z. Cao, M. X. Li, X. D. Duan and J. W. Hu, *J. Mater. Chem. A*, 2020, **8**, 21062–21069.
156 X. Zhu, M. Liu, X. Qi, H. Li, Y. F. Zhang, Z. Li, Z. Peng, J. Yang, L. Qian, Q. Xu, N. Gou, J. He, D. Li and H. Lan, *Adv. Mater.*, 2021, **33**, e2007772.
157 X. C. Meng, Y. F. Xu, Q. X. Wang, X. Yang, J. M. Guo, X. T. Hu, L. C. Tan and Y. W. Chen, *Langmuir*, 2019, **35**, 9713–9720.
158 Z. L. Zhang, X. Y. Zhang, Z. Q. Xin, M. M. Deng, Y. Q. Wen and Y. L. Song, *Adv. Mater.*, 2013, **25**, 6714–6718.
159 X. He, G. Z. Shen, R. B. Xu, W. J. Yang, C. Zhang, Z. H. Liu, B. H. Chen, J. Y. Liu and M. X. Song, *Polymers*, 2019, **11**, 468.
160 M. Ohsawa and N. Hashimoto, *Microelectron. Reliab.*, 2019, **98**, 124–130.
161 M. Ohsawa and N. Hashimoto, *Mater. Res. Express*, 2018, **5**, 085030.
162 H. Wu, D. S. Kong, Z. C. Ruan, P. C. Hsu, S. Wang, Z. F. Yu, T. J. Carney, L. B. Hu, S. H. Fan and Y. Cui, *Nat. Nanotechnol.*, 2013, **8**, 421–425.
163 S. R. Chen, M. Su, C. Zhang, M. Gao, B. Bao, Q. Yang, B. Su and Y. L. Song, *Adv. Mater.*, 2015, **27**, 3928.
164 B. Bao, J. K. Jiang, F. Y. Li, P. C. Zhang, S. R. Chen, Q. Yang, S. T. Wang, B. Su, L. Jiang and Y. L. Song, *Adv. Funct. Mater.*, 2015, **25**, 3286–3294.
165 Z. W. Wu, P. Li, Y. K. Zhang and Z. J. Zheng, *Small Methods*, 2018, **2**, 1800031.
166 H. S. Jung, G. S. Han, N.-G. Park and M. J. Ko, *Joule*, 2019, **3**, 1850–1880.
167 J. B. Tian, Z. X. Lin, Z. Y. Chen, S. N. Obaid, I. R. Efimov and L. Y. Lu, *Photonics*, 2021, **8**, 220.
168 X. Lu, Y. K. Zhang and Z. J. Zheng, *Adv. Electron. Mater.*, 2021, **7**, 2001121.
169 B. Dou, E. M. Miller, J. A. Christians, E. M. Sanehira, T. R. Klein, F. S. Barnes, S. E. Shaheen, S. M. Garner, S. Ghosh, A. Mallick, D. Basak and M. van Hest, *J. Phys. Chem. Lett.*, 2017, **8**, 4960–4966.
170 K.-G. Lim, T.-H. Han and T.-W. Lee, *Energy Environ. Sci.*, 2021, **14**, 2009–2035.

171 K. Zilberberg and T. Riedl, *J. Mater. Chem. A*, 2016, **4**, 14481–14508.
172 H. Hu, S. Zhao, W. S. Wang, Y. Q. Zhang, Y. Fu and Z. J. Zheng, *Appl. Phys. Lett.*, 2021, **119**, 071603.
173 X. Z. Dai, Y. H. Deng, C. H. Van Brackle, S. S. Chen, P. N. Rudd, X. Xiao, Y. Lin, B. Chen and J. S. Huang, *Adv. Energy Mater.*, 2020, **10**, 1903108.
174 D. Zhang, Y. Liu, Y. Liu, Y. Peng, Y. Tang, L. Xiong, X. Gong and J. Zheng, *Adv. Mater.*, 2021, **33**, 2104006.
175 M. Wong-Stringer, T. J. Routledge, T. McArdle, C. J. Wood, O. S. Game, J. A. Smith, J. E. Bishop, N. Vaenas, D. M. Coles, A. R. Buckley and D. G. Lidzey, *Energy Environ. Sci.*, 2019, **12**, 1928–1937.
176 B. Hwang, C. H. An and S. Becker, *Mater. Des.*, 2017, **129**, 180–185.
177 S. Kang, J. Jeong, S. Cho, Y. J. Yoon, S. Park, S. Lim, J. Y. Kim and H. Ko, *J. Mater. Chem. A*, 2019, **7**, 1107–1114.
178 W. Y. Jin, R. T. Ginting, K. J. Ko and J. W. Kang, *Sci. Rep.*, 2016, **6**, 36475.
179 H.-G. Im, S. Jeong, J. Jin, J. Lee, D.-Y. Youn, W.-T. Koo, S.-B. Kang, H.-J. Kim, J. Jang, D. Lee, H.-K. Kim, I.-D. Kim, J.-Y. Lee and B.-S. Bae, *NPG Asia Mater.*, 2016, **8**, e282.
180 H. Dong, Z. Wu, Y. Jiang, W. Liu, X. Li, B. Jiao, W. Abbas and X. Hou, *ACS Appl. Mater. Interfaces*, 2016, **8**, 31212–31221.
181 M. Xie, J. Wang, J. Kang, L. Zhang, X. Sun, K. Han, Q. Luo, J. Lin, L. Shi and C.-Q. Ma, *Flexible Printed Electron.*, 2019, **4**, 034002.
182 P. Li, Z. Wu, H. Hu, Y. Zhang, T. Xiao, X. Lu, Z. Ren, G. Li, Z. Wu, J. Hao, H.-L. Zhang and Z. Zheng, *ACS Appl. Mater. Interfaces*, 2020, **12**, 26050–26059.
183 G. Xu, R. Xue, W. Chen, J. Zhang, M. Zhang, H. Chen, C. Cui, H. Li, Y. Li and Y. Li, *Adv. Energy Mater.*, 2018, **8**, 1703054.
184 H. B. Michaelson, *J. Appl. Phys.*, 1977, **48**, 4729–4733.
185 S. Kundu and T. L. Kelly, *EcoMat*, 2020, **2**, e12025.
186 X. D. Li, S. Fu, W. X. Zhang, S. Z. Ke, W. J. Song and J. F. Fang, *Sci. Adv.*, 2020, **6**, eabd1580.
187 T. Zhu, Y. Yang, S. Zhou, X. Yao, L. Liu, W. Hu and X. Gong, *Chin. Chem. Lett.*, 2020, **31**, 2249–2253.
188 F. Igbari, M. Li, Y. Hu, Z.-K. Wang and L.-S. Liao, *J. Mater. Chem. A*, 2016, **4**, 1326–1335.
189 Q. Jiang, L. Zhang, H. Wang, X. Yang, J. Meng, H. Liu, Z. Yin, J. Wu, X. Zhang and J. You, *Nat. Energy*, 2016, **2**, 16177.
190 E. Lee, J. Ahn, H.-C. Kwon, S. Ma, K. Kim, S. Yun and J. Moon, *Adv. Energy Mater.*, 2018, **8**, 1702182.
191 J. Han, S. Yuan, L. Liu, X. Qiu, H. Gong, X. Yang, C. Li, Y. Hao and B. Cao, *J. Mater. Chem. A*, 2015, **3**, 5375–5384.
192 M. Vasiliev, M. Nur-E-Alam and K. Alameh, *Energies*, 2019, **12**, 1080.
193 W. S. Subhani, K. Wang, M. Du, X. Wang, N. Yuan, J. Ding and S. Liu, *J. Energy Chem.*, 2019, **34**, 12–19.
194 H. Dinesh and J. M. Pearce, *Renewable Sustainable Energy Rev.*, 2016, **54**, 299–308.
195 K. S. Chen, J. F. Salinas, H. L. Yip, L. J. Huo, J. H. Hou and A. K. Y. Jen, *Energy Environ. Sci.*, 2012, **5**, 9551–9557.
196 M. Mujahid, C. Chen, J. Zhang, C. Li and Y. Duan, *InfoMat*, 2021, **3**, 101–124.
197 F. Guo, H. Azimi, Y. Hou, T. Przybilla, M. Y. Hu, C. Bronnbauer, S. Langner, E. Spiecker, K. Forberich and C. J. Brabec, *Nanoscale*, 2015, **7**, 1642–1649.
198 X. Dai, Y. Zhang, H. Shen, Q. Luo, X. Zhao, J. Li and H. Lin, *ACS Appl. Mater. Interfaces*, 2016, **8**, 4523–4531.
199 H. Hwang, A. Kim, Z. Zhong, H.-C. Kwon, S. Jeong and J. Moon, *Adv. Funct. Mater.*, 2016, **26**, 6545–6554.